Iranian Journal of Science and Technology, Transactions of Civil Engineering (2020) 44:299–315
https://doi.org/10.1007/s40996-019-00259-x

RESEARCH PAPER

Comparison of Experimental and Numerical Model Results of Oscillating Water Column System Under Regular Wave Conditions

Farrokh Mahnamfar[1] · Abdüsselam Altunkaynak[2] · Yasin Abdollahzadehmoradi[3]

Received: 30 July 2017 / Accepted: 19 March 2019 / Published online: 30 March 2019

Abstract

Wave energy has attracted significant attention because of its non-polluting nature, environment friendliness, low operational cost and simple maintenance procedures compared to other clean energy sources. In this study, it was attempted to optimize an oscillating water column (OWC) wave energy converter, which is constructed on a shoreline. This study proposed numerical and physical models for the optimization of the OWC-type wave energy converters. Sixty-four experimental sets were carried out by a piston-type wave maker in order to investigate the influence of wave parameters, water depth and geometry of coastal structures on the efficiency of the system. A numerical model of the experimental model sets of the OWC system was performed by a software called Flow 3D. Intersection with a water–air in the software for the determination of the free surface of a volume of fluid method is used. K–ε turbulence model was used for turbulent model. The drag coefficient, surface roughness, pipe roughness and surface tension were used for calibration. It is observed that the numerical model results follow the experimental model results. The numerical and the experimental model results were compared with each other by taking into consideration the mean squared error, coefficient of determination (R^2) and Nash–Sutcliffe efficiency (NSE) as performance evaluation criteria. According to the test results, the NSE value was obtained to be 0.97 and this value also shows very good agreement between numerical results and experimental results. The experimental results showed that wave parameters are strongly related to the outflow of air from the chamber, whereas the slope angle of the chamber is inversely related. Considering different water depths, the various wave series and angle of the chamber, maximum efficiency of OWC was obtained at 50 cm, wave series No. 1 and an angle of 40°, respectively.

Keywords Wave energy · Wave energy converters · Experimental testing · Numerical modeling · Performance evaluation criteria · OWC

Abbreviations

CFD	Computational fluid dynamics
FAVOR	Fractional area/volume obstacle representation
LIMPET	Land installed marine powered energy transformer
NS	Navier–Stokes
MSE	Mean square error
NSE	Nash–Sutcliffe coefficient
OWC	Oscillating water column
RANS	Reynolds-averaged Navier–Stokes
REWEC	Resonant wave energy converter
VOF	Volume of fluid

List of Symbols

A	The cross-sectional area of the outflow air tube
A_x	Fractional area at the centers of cell faces normal to the x-direction
A_y	Fractional area at the centers of cell faces normal to the y-direction
A_z	Fractional area at the centers of cell faces normal to the z-direction

✉ Farrokh Mahnamfar
fmahnamfar@sakarya.edu.tr

Abdüsselam Altunkaynak
altunkay@itu.edu.tr

Yasin Abdollahzadehmoradi
yabdullahzade@gelisim.edu.tr

[1] Faculty of Engineering, Department of Civil Engineering, Sakarya University, 54187 Adapazarı, Sakarya, Turkey

[2] Faculty of Civil Engineering, Hydraulics Division, Istanbul Technical University, 34469 Maslak, Istanbul, Turkey

[3] Faculty of Engineering and Architecture, Istanbul Gelisim University, Avcilar, Istanbul, Turkey

$C_{1\varepsilon}$, $C_{2\varepsilon}$, $C_{3\varepsilon}$	Constant values
D	Diameter of air outflow tube
Diff	Diffusion term
d	Water depth
E	Mean air velocity from the results of experimental model
$\bar{E}$	Mean of E values
e	Height of opening of the OWC front wall
F	Fraction of fluid in each cell
f_x	Viscous acceleration in x-direction
f_y	Viscous acceleration in y-direction
f_z	Viscous acceleration in z-direction
G_k	Buoyancy production term
G_x	Body accelerations in the x-direction
G_y	Body accelerations in the y-direction
G_z	Body accelerations in the z-direction
H	Incident wave height
k	Kinetic energy of turbulent
L	Wavelength
N	Mean air velocity from the results of numerical model
$\bar{N}$	Mean of N values
P	Pressure
P_{k}	Turbulent kinetic energy production
P_{owc}	Power of output air
Q	Air discharge
R^2	Coefficient of determination
Re	Reynolds number
R_{SOR}	Mass source
T	Wave period
t	Time
u	Velocity component in x-direction
V	Velocity of air flow
v	Velocity component in y-direction
V_f	Volumetric fluid fraction in each cell
w	Velocity component in z-direction
X	Front wall length of oscillating water column system
x	Coordinate in x-direction
$x_{\max}$	Downstream boundary condition
$x_{\min}$	Upstream boundary condition
y	Coordinate in y-direction
Z	Elevation head
z	Coordinate in z-direction (m)
$z_{\max}$	Upper limit of the solution
$z_{\min}$	Base wall
α	Front wall angle of oscillating water column system
γ	Specific weight
ΔP	Differential pressure
ε	Dissipation rate of turbulent kinetic energy (k–ε model)
μ_{a}	Dynamic viscosity of air
ρ	Density
ρ_{a}	Density of air
ρ_{w}	Density of water
ω	Specific dissipation rate of turbulent kinetic energy ($k-\omega$ model)

1 Introduction

The oceans have enormous wave energy potential that is spread along the world's coastlines. It has been estimated that the practical annual world wave energy resource is somewhere between 2000 and 4000 TWh. In order to put this into perspective, this equates to a value of approximately 20% of the world's electricity production in the year 2003 (International Energy Agency 2005). Sağlam et al. (2010) studied the wave energy potential of the Black sea and Aegean Regions of Turkey. The study showed that west of the Black Sea in the north of Istanbul Straits and the region off the southwestern and western coasts of Aegean Region of Turkey as the best productive sites for converting wave energy into electricity. It was also found that the estimated annual technical wave energy potential of Turkey is 10 TWh with the annual wave power ranging between 3 and 17 kW/m.

The research and development (R&D) work on OWC-type wave energy plants has been primarily based on simplified analytical models. In this area, Evans (1982) characteristically assumed a simplified "rigid piston" approach to the modeling of the free surface inside the OWC system and/or the interface below the lip of the front wall of OWC. The results are based on classical linear water wave theory and show the close analogies which exist with theories for systems of absorbing oscillatory rigid bodies. In addition, a number of new reciprocal relations for pressure distributions are suggested and proved.

Prior to the full-scale fabrication of existing prototype plants, mathematical models were used in order to specify initial OWC design parameters (i.e., key geometric dimensions, turbine parameters), which were experimentally optimized, tested and verified prior to implementation in the prototypes (Joyce et al. 1993).

Purely numerical studies were undertaken using a numerical wave tank (Clément 1996) in order to determine the influence of geometric parameters on the nonlinear radiation response of an OWC system. Tindall and Xu (1996) performed an optimization study to investigate the effects of the power takeoff turbine.

Three-dimensional (3D) numerical studies were conducted using commercially available hydrodynamic radiation–diffraction models developed for the analysis of floating bodies (Brito-Melo et al. 1999). The models were developed to predict accurately the hydrodynamic behavior of the OWC system. However, the implementation of the OWC analysis required considerable modification of the software. In

addition, an extensive knowledge of computer programming and access to the source code were required.

Folley et al. (2006) compared the performance of Wells turbine installed in the LIMPET system with theoretical analysis and model tests. The dimensions of the water column of the LIMPET system are 3.6 m×6 m and feed a pair of 2.6-m-diameter contra-rotating Wells turbine, each of which drives a 250 kW generator. Martins et al. (2005) presented an OWC wave energy system by incorporating the OWC chamber into a breakwater with the objective of reducing the cost of the chamber and commercializing the technology.

Hong et al. (2007) evaluated how several shape parameters of the OWC chamber affect its wave energy absorbing capability. El Marjani et al. (2008) conducted a numerical model with the objective of forecasting flow characteristics in the components of an OWC system for capturing the wave energy.

Josset and Clément (2007) carried out a study using the low-order boundary element method to obtain efficient hydrodynamic modeling of generic bottom mounted OWC converter. An experimental study was conducted by Morris-Thomas et al. (2007) with the objective of evaluating the hydrodynamic performance of an OWC analyzing the influence of the lip configuration including depth, thickness and geometry. Dizadji and Sajadian (2011) conducted a series of wave flume tests in order to modify the slope of the front and rear walls of a small-scale OWC model searching for optimal geometry. Zhang et al. (2012) developed a 2D-RANS model to investigate wave interaction and studied the vortical motion around the OWC chamber. They researched the effect of chamber geometry parameters of the OWC system on energy efficiency of the OWC model. They found a good agreement between their experimental results and the experimental results of other studies in the literature.

Tseng et al. (2000) developed a wave converter system which combined the concept of a breakwater and a harbor resonance chamber. A physical model was established with a scale of 1:20, and the model was tested in the wave tank. A comparison between the experimental data and the previous theoretical results was performed. Wang et al. (2002) constructed a physical model with different bottom slopes and investigated topographical effects of the bottom slope on hydrodynamic performance of OWC system under regular wave conditions. In addition, they validated numerical computations in comparison with experimental data of the chamber wave amplification factors. They showed the importance of localized effect on the overall efficiency of the system. Boccotti (2007) patented a new model of OWC form, known as resonant wave energy converter (REWEC). The scale of the designed model was 1:10, and a small Wells turbine was tested in this experiment. Liu et al. (2008) used a numerical technique to simulate the fluid dynamic behavior of the OWC system. They established a numerical wave tank by CFD code to generate the propagating waves. Good agreement was observed between the numerical model results of the OWC and published experimental data. Also, Marjani et al. (2008) studied the flow characteristics in the components of OWC system. The numerical simulation tool was used to predict flow characteristics inside the OWC system. Malara and Arena (2013) introduced a new OWC system called U-OWC. This device is different from the traditional OWC system, and a small vertical U-duct is used to connect the air pocket to the environment. The purpose of their study was to consistently represent the wave field that interacts with the U-OWC and produces equation of motion of OWC. Nonlinear differential equation was used to define U-OWC dynamics. In the next step, Monte Carlo simulations were employed for evaluating the performance of the U-OWC device in random waves. Performance of the U-OWC was investigated with four different types of Wells turbines.

The effect of geometry and dimensions of the OWC chamber on the efficiency of the OWC system was investigated, and the geometry of the system was optimized to achieve the maximum power by Bouali and Larbi (2013). ANSYS-ICEM CFD was used for geometry and meshing. Using the ANSYS-CFX software, flow field equations were solved. The best shape regarding the unit efficiency was obtained at the air chamber front wall in the counter-flow direction at 180° angle. As a result of this study, the optimal value of the front wall immersion depth was found to be between 0.38 and 0.44 times the water depth and the best dimension was found to be between 0.8 and 1 times the water depth. Texeira et al. (2013) analyzed front wall depth, length and height of oscillating water column chamber and turbine characteristics. They performed numerical simulations by means of Navier–Stokes (NS) equations and applied semi-implicit two-step Taylor–Galerkin method. Fluinco and the commercial fluent model were compared with each other, and a good agreement was observed between these models. Luo et al. (2014) applied 2D fully nonlinear Euler model using ANSYS Fluent software to analyze the efficiency of fixed OWC wave energy converter. This model was compared to other numerical models and experimental research results. The results showed the presence of good agreement between the simulation results for OWC and the analytical theory of Sarmento and Falcao (1985) for linear waves. The most important result of their research is that hydrodynamic capture efficiency of the OWC system tent decreases significantly with increasing wave height. Ramandan et al. (2014) constructed a numerical model for the wave energy conversion system. In the study, a new float was designed and its performance was analyzed analytically. The float was formed from a hallow cylinder and inverted cup. The developed model results were validated by experimental

results for the same data sets. The new float was compared with the conventional float in terms of mechanism of transmission and power production. As a result, the new float was found to produce higher power than the conventional float.

One of the most widely used and investigated systems around the world is the OWC system. For this reason, our research has focused on this system. This system generates energy by compressing air in the water column and transmits the air on the water column to the turbines. The objective of this study was to develop a numerical model that can be used to optimize an OWC system and to test the optimized numerical model results with physical model by experiments. FLOW-3D software was used for numerical simulation. FLOW-3D is a commercial CFD tool that gives engineers valuable insight into many physical flow processes. This software has special capabilities for accurately predicting free surface flows. For example in free surface flow, FLOW-3D software was used for numerical modeling of cavitation on spillway's flip bucket by Parsaie et al. (2016) and numerical modeling of flow pattern in dam spillway's guide wall by Dehdar-Behbahani and Parsaie (2016). In this study, the air flow was measured by Pitot tube. For each experimental group, the velocities of air at the outflow and wave heights were measured for the four different regular wave series and four different water depths. In this study, the air flow was measured using different methods and the OWC structure is designed to have different geometry from other studies in the literature. In addition, the numerical and experimental model results of air flow were analyzed and compared with each other. In many other studies, just numerical or experimental models were analyzed with limited geometry form of OWC structure.

2 Experimental Setup and Hydraulic Model Tests

Two-dimensional (2D) experimental research was conducted in the wave flume of Hydraulics Laboratory of Istanbul Technical University. The wave channel is 22 m long and 1 m wide with 1 m depth as shown in Fig. 1. The windows at the flume wall are transparent in order to observe the wave propagation and raised water level in the OWC structure interaction. The experimental setup included wave generator (maker) at the beginning of channel and the OWC structure at the end of channel.

In this study, the effects of the front slope angle of the breakwater, which were given as 47°, 40°, 35° and 30°, the incident wave height (H) and wave period (T), which were in the ranges of 8–20 cm and 0.8–2.3 s, respectively, and the mean water depths (d), which were given as 30, 40, 50 and 60 cm, were investigated. We are set to ensure consistent wave condition for all test series.

A wave-absorbing porous beach with a slope of 1:4 was also deployed at the end of the channel. The wave propagation in the channel and oscillatory air outflow from the chamber were assessed. The wave propagation was measured with capacitance-type wave gages. In addition, the velocity from the chamber was measured and registered with the help of Pitot tube equipped using a digital manometer. The measurements were then interpreted to optimize the geometry of the chamber to harvest wave energy.

(a) Side view **(b)** plan view

Fig. 1 Wave flume in Hydraulics Laboratory of Istanbul Technical University

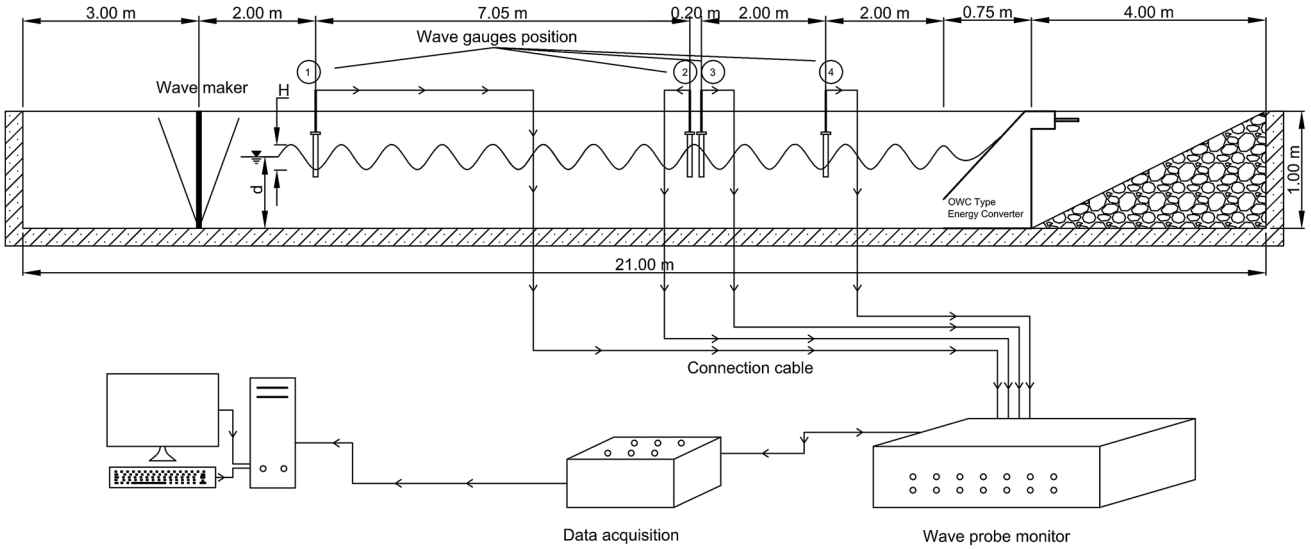

Fig. 2 Sketch of the wave flume with wave gauges location

Fig. 3 OWC system with a width of 50 cm

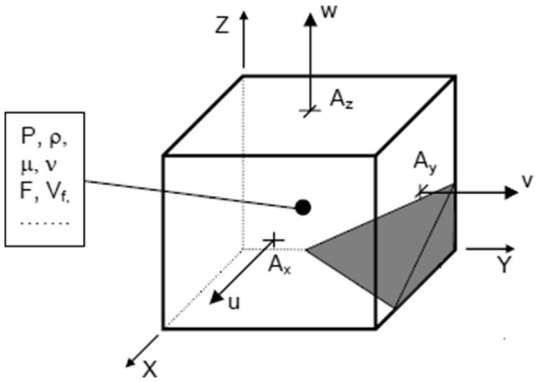

Fig. 4 Representation of variables that affect a cell calculation

In this study, 64 experimental data sets were generated by a piston-type wave maker. The free surface in front of the structure was measured by four capacitance wave gauges. Pitot tube equipped with a digital manometer was installed at the rear side of the chamber. The data rate (sampling rate) was taken as 10 units per second for wave measurements. A configuration of the wave flume and the location of the gauges are shown in Fig. 2.

Wave characteristics were generated by the first wave gauge; the reflection analysis was made by the wave gauges 2 and 3; and measurement of wave height just in front of the structure was performed by wave gauge 4.

In this study, the chamber of the OWC system was constructed with plywood as shown in Fig. 3.

Plexiglas was used on the one side which enables to see the variations of the water fluctuations in the system. The chamber was sealed that no additional air and water infiltrations are allowed. A tube was mounted at the rear of the chamber to measure the air inflow and outflow discharge.

3 Numerical Simulation

In this study, the computations for the flow were made by using software called FLOW-3D assuming steady flow conditions and taking fluids as incompressible.

The governing equations are continuity and the Reynolds-averaged Navier–Stokes (RANS) equations. Three-dimensional motion and RANS equations are used for the solution of these equations with finite volume methods. Rectangular cells were used in order to obtain a non-uniform mesh for computations. Velocities (u, v, w) on the surface of the control volume

scalars (cells) as well as the fluid pressure, density, viscosity are taken into account (Fig. 4).

Fluid velocities and pressures are located at staggered mesh locations for a typical cell as shown in Fig. 4: u is velocity component in the x-direction and A_x is fractional area at the centers of cell faces normal to the x-direction, v is velocity component in the y-direction and A_y is fractional area at the centers of cell faces normal to the y-direction, and w is velocity component in the z-direction and A_z is fractional area at the centers of cell faces normal to the z-direction. Rectangular grids are very easy to generate and store because of their regular, or structured, nature. A non-uniform grid spacing adds flexibility when meshing complex flow domains. Structured rectangular grids have advantages, such as partial easiness in the development of numerical methods, clarity of the last concerning their connection to the original physical problem, and in the end, precision and integrity of the numerical solutions.

Intersection with a water–air in the software for the determination of the free surface of a volume of fluid (VOF) method is used. VOF method is similar to the FAVOR approach (fractional area/volume obstacle representation) of empty cells which are determined to be fully or partially filled with water. In this method, fraction of fluid in each cell is represented by a function F. The average value of F in a cell would then represent the fractional volume of the cell occupied by fluid. For the cell filled with liquid completely, F is equal to 1. For the empty cell, F is equal to 0. Cells with F values between zero and one must then contain a free surface. This equation states that F moves with the fluid and is the partial differential equation analog of marker particles. Fluid volume variation can be written in a mathematical form as follows (Flow Science Inc. 2012):

$$\frac{\partial F}{\partial t} + u\frac{\partial F}{\partial x} + v\frac{\partial F}{\partial y} + w\frac{\partial F}{\partial z} = 0 \tag{1}$$

Reynolds-averaged Navier–Stokes equations

Three-dimensional continuity and movement equations in Cartesian coordinates are written for incompressible flow as follows:

$$V_f\frac{\partial \rho}{\partial t} + \frac{\partial}{\partial x}(uA_x) + \frac{\partial}{\partial y}(vA_y) + \frac{\partial}{\partial z}(wA_z) = \frac{R_{\mathrm{SOR}}}{\rho} \tag{2}$$

$$\begin{aligned}
&\frac{\partial u}{\partial t} + \frac{1}{V_f}\left(uA_x\frac{\partial u}{\partial x} + vA_y\frac{\partial u}{\partial y} + wA_z\frac{\partial u}{\partial z}\right) = -\frac{1}{\rho}\frac{\partial p}{\partial x} + G_x + f_x\\
&\frac{\partial v}{\partial t} + \frac{1}{V_f}\left(uA_x\frac{\partial v}{\partial x} + vA_y\frac{\partial v}{\partial y} + wA_z\frac{\partial v}{\partial z}\right) = -\frac{1}{\rho}\frac{\partial p}{\partial y} + G_y + f_y\\
&\frac{\partial w}{\partial t} + \frac{1}{V_f}\left(uA_x\frac{\partial w}{\partial x} + vA_y\frac{\partial w}{\partial y} + wA_z\frac{\partial w}{\partial z}\right) = -\frac{1}{\rho}\frac{\partial p}{\partial z} + G_z + f_z.
\end{aligned} \tag{3}$$

Here, u, v and w are the velocity components (m/s) in the x-, y- and z-directions, respectively, A_x, A_y and A_z are similar area fractions for flow in the x-, y- and z-directions, respectively, ρ is the fluid density (kg/m^3), R_{SOR} is a mass source, P is the pressure (kg/(m s^2)), V_F is the fractional volume open to flow, G_x, G_y and G_z are body accelerations (m/s^2) in the x-, y- and z-directions, respectively, f_x, f_y and f_z are viscous accelerations (m/s^2) in the x-, y- and z-directions, respectively.

The Prandtl mixing length model, the one-equation, the two-equation k–ε and RNG models, and a large eddy simulation model are five turbulence models are used in FLOW-3D. The K–ε model was used in this study because it provides reasonable approximations to many flow types and it is the most common model used in computational fluid dynamics. The Reynolds stresses are modeled by the standard two-equation k–ε turbulence model. In this model, kinetic energy "k" and dissipation rate "ε" are written as:

$$\frac{\partial k}{\partial t} + \frac{1}{V_F}\left[uA_x\frac{\partial k}{\partial x} + vA_y\frac{\partial k}{\partial y} + wA_z\frac{\partial k}{\partial z}\right] = P_k + G_k + \mathrm{Diff} - \varepsilon \tag{4}$$

$$\begin{aligned}
&\frac{\partial \varepsilon}{\partial t} + \frac{1}{V_F}\left[uA_x\frac{\partial \varepsilon}{\partial x} + vA_y\frac{\partial \varepsilon}{\partial y} + wA_z\frac{\partial \varepsilon}{\partial z}\right]\\
&= \frac{C_{1\varepsilon}.\varepsilon}{k}\left(P_k + C_{3\varepsilon}.G_k\right) + \mathrm{Diff}_\varepsilon - C_{2\varepsilon}.\frac{\varepsilon^2}{k}
\end{aligned} \tag{5}$$

Here, P_k is turbulent kinetic energy production, G_k is buoyancy production term, Diff and Diff$_\varepsilon$ demonstrate diffusion term, and $C_{1\varepsilon}$, $C_{2\varepsilon}$, $C_{3\varepsilon}$ are constant values. $C_{1\varepsilon}$ and $C_{2\varepsilon}$ for standard k–ε model are selected as 1.44 and 1.92, respectively.

In the software, the three-dimensional, single-precision, implicit, segregated solver was selected. In addition,

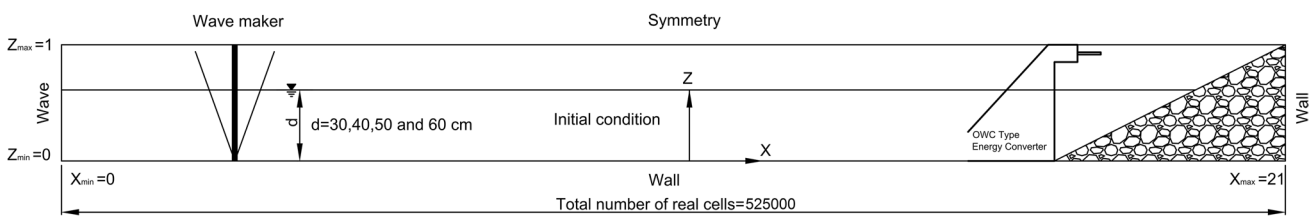

Fig. 5 Geometry and boundary conditions of solution domain (RANS) (dimensions in meter)

a second-order implicit time discretization, with a time step of 0.01 s and a maximum of 100 iterations per time step, was used for the flow simulation. Moreover, the fluid was assumed to be air with constant properties of $\rho_a = 1.225$ kg/m^3 and $\mu_a = 1.789 \times 10^{-5}$ kg/m s (Flow Science Inc. 2012).

The computational domain was defined as 1 m depth, 1 m width and 21 m length for RANS (Fig. 5) as channel dimensions. A volume of fluid with depths of 0.30, 0.40, 0.50 and 0.60 m, width of 1 m and length of 21 m was set as initial condition to represent the wave flume.

Upstream boundary condition (x_{min}), which was taken as the wave channel, is handled as a manufacturer of wave, and the downstream boundary condition (x_{max}) is designated as the wall. Wave boundary condition applies the velocity field associated with the requested wave type. No slip condition was applied to the wall. Thus, it is assumed that horizontal and vertical velocities at the surface of the wall are zero. The upper limit of the solution (z_{max}) was taken as the symmetry where the free water surface atmospheric pressure can be effective, and this boundary condition applies a zero-gradient condition at the boundary as well as a zero-velocity condition normal to the boundary. Free surface was defined with the search on the water–air cross section of VOF boundary condition in which zero shear stress and constant pressure were applied by the software. The channel was taken as the base (z_{min}) wall. Because the k–ε turbulence model in solving RANS wall function equations is given in the previous section, the software uses the speed distribution (Flow Science Inc. 2012).

Numerical solutions in studies of selected numerical results on the mesh spacing can be quite effective. Therefore, in order to determine the appropriate range of different mesh sizes, a preliminary study using mesh ranges and how it affects the free surface profile were analyzed (Fig. 6).

FLOW-3D program performs computations only on network of rectangular cells. In RANS solution, a mesh of fixed rectangular cells with Cartesian coordinates was used and uniform mesh size was taken over the whole computational domain. Therefore, for x- and z-directions, the meshes are considered to be 0.02 m in size and the y-direction was divided into 10 parts and the mesh size was 0.05 m. Drag coefficient and surface roughness were considered for wave flume in the FLOW-3D software (Flow Science Inc. 2012). The losses between the structure's wall and air, the structure's wall and water and the output pipe are considered in numerical models. Changing these values, close values to the experimental results have been obtained and then these coefficient values are found. All the equations given in the numerical simulation section are taken from FLOW-3D User's Manuals (Flow Science Inc. 2012).

4 Experimental Method

It is well known that the more the outflow air discharge, the more the energy that is harvested. For this reason, the parameters mentioned below were used in order to obtain the maximum outflow discharge of air. In this study, the parameters including water wave height (H), wavelength (L), wave period (T), water depth (d), the velocity of air flow (V), air discharge (Q), differential pressure (ΔP), air density (ρ_a), dynamic viscosity of air (μ_a), diameter of air outflow tube (D) and the power of output air (P_{owc}) were considered.

The main purpose of this study was to obtain the optimum design of chamber geometry by changing the dimensions and

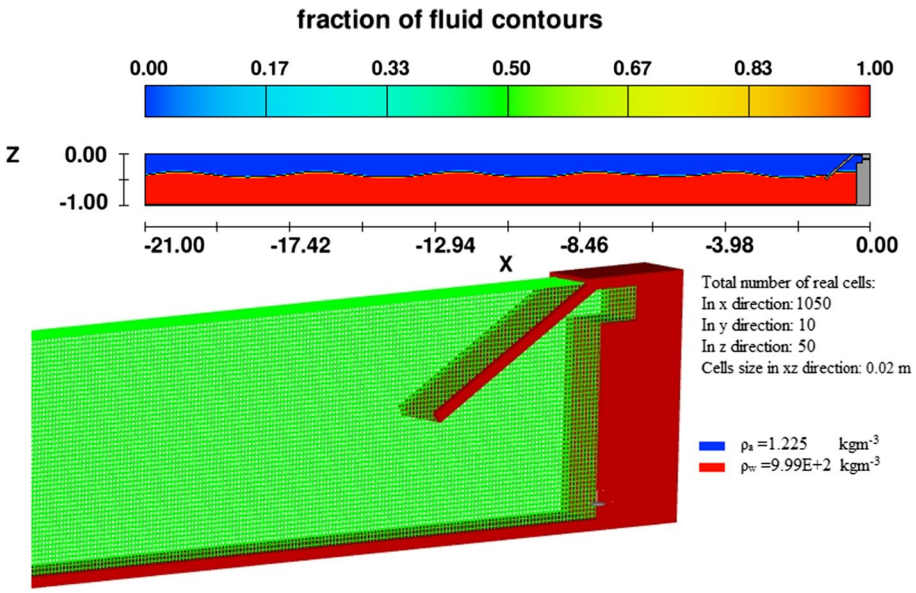

Fig. 6 Mesh of the OWC system

front angles. The structure was placed in an open channel, and regular wave conditions were generated. The Reynolds number (*Re*) in outlet tube was calculated using the following equation:

$$Re = \left(\frac{\rho VD}{\mu_a}\right) \tag{6}$$

where V is the velocity of outflow air (m/s), D is the diameter of outflow air tube (m), ρ_a is the air density (kg/m^3), and μ_a is the dynamic viscosity of air (kg/m s).

A general equation of a wavelength (L) depends on parameters of water depth (d) and wave period (T), and the expression can be written as follows (Shore Protection Manual 1984):

$$L = \left(\frac{gT^2}{2\pi}\right)\tanh\left(\frac{2\pi d}{L}\right) \approx \frac{gT^2}{2\pi}\sqrt{\tanh\left(\frac{4\pi^2}{T^2}.\frac{d}{g}\right)} \tag{7}$$

where g is the gravity acceleration.

The expression of wavelength for shallow water can be written as follows:

$$L = T\sqrt{gd} \tag{8}$$

Wavelength for deep water can be calculated from Eq. 9 (Shore Protection Manual 1984):

$$L = \frac{gT^2}{2\pi} \tag{9}$$

Bernoulli's equation can be defined for Pitot tube as:

$$\frac{P}{\gamma} + \frac{V^2}{2g} + Z = \text{Constant} \tag{10}$$

Applying Bernoulli's equation at two different points along a streamline can be written as:

$$\frac{P_1}{\gamma} + \frac{V_1^2}{2g} + Z_1 = \frac{P_2}{\gamma} + \frac{V_2^2}{2g} + Z_2 \tag{11}$$

As $Z_1 = Z_2$ and point 2 is a stagnation point, $V_2 = 0$. Therefore, Eq. (11) can be reduced as:

$$\frac{P_1}{\gamma} + \frac{V_1^2}{2g} = \frac{P_2}{\gamma} \tag{12}$$

$$\frac{P_2 - P_1}{\rho g} = \frac{V_1^2}{2g} \tag{13}$$

Finally, change in pressure (ΔP) was calculated using the Bernoulli equation given as:

$$\Delta P = \left(\frac{\rho V^2}{2}\right) \tag{14}$$

where ΔP is differential pressure. Knowing cross-sectional area (A) of the outflow air tube, the air discharge can be calculated. This experiment was taken under four groups of experimental sets based on variety of α, e and X values, which are depicted in Fig. 7.

For each experimental group, the velocity of air at the outflow and wave height were measured for the four different regular wave series and four different water depths, which are described in Sect. 2 (a total of $4\times4\times4=64$ data sets were generated). Then, 64 ΔP versus t diagrams were plotted to indicate time (t) versus the variation of ΔP. In addition, the maximum and the mean values of air velocity at the outflow tube and air flow discharge, and mean change in pressure were presented in tables in Sect. 6. The results of the optimum solutions for energy harvesting are tabulated in Sect. 6.

The absorbed power is determined based on the water column's heave velocity, as determined from the derivative of the displacement signal. The power of output air P_{owc} from chamber is computed as:

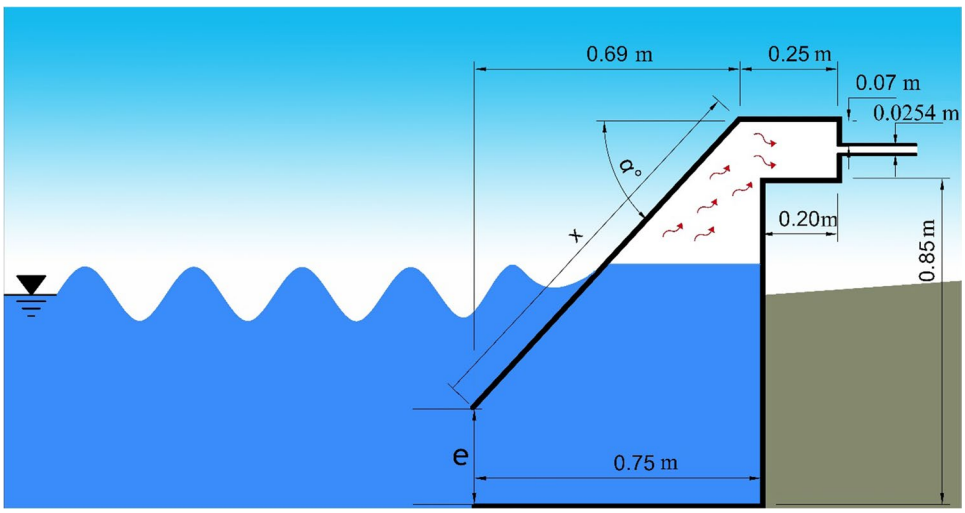

Fig. 7 Cross section of the OWC system

$$P_{\text{owc}} = \Delta P.V.A \tag{15}$$

where

$$P_{\text{owc}} = V\left(\rho\frac{V^2}{2}\right)\left(\frac{\pi D^2}{4}\right) \tag{16}$$

Here, P_{owc} is the power of output air (W), ρ_{a} is the air density (kg/m^3), V is the outflowing air velocity (m/s), and D is the diameter of the outflow air tube (m).

The average wave power (P_w) can be expressed as (Warner 1997):

$$P_w = \frac{1}{32\pi}\rho_w g^2 H^2 T.b \tag{17}$$

where P_w is the power of wave (kw), ρ_{w} is the water density (kg/m^3), H is the wave height (m), wave period (s), width of wave crest (m).

We defined a dimensionless number, η, which is the ratio of the power of OWC (P_{owc}) to wave power (P_w).

5 Evaluation Criteria

In this study, two types of evaluation criteria were used to illustrate the relationship between numerical model results and experimental data. These two criteria used to evaluate the performance of the models are coefficient of determination and Nash–Sutcliffe efficiency (Krause et al. 2005).

5.1 Coefficient of Determination (R^2)

Correlation coefficient measures linear dependence between two random variables such as numerical model results versus experimental model results. The correlation coefficient is calculated by the following equation:

$$R^2 = \left(\frac{\sum_{i=1}^{n}\left(E_i-\bar{E}\right)\left(N_i-\bar{N}\right)}{\sqrt{\sum_{i=1}^{n}\left(E_i-\bar{E}\right)^2}\sqrt{\sum_{i=1}^{n}\left(N_i-\bar{N}\right)^2}}\right)^2 \tag{18}$$

where E is the mean air velocity from the results of experimental model; N is the mean air velocity from the results of numerical model; $\bar{E}$ is the mean of E values, and $\bar{N}$ is the mean of N values.

The coefficient of determination is in the range of $0 < R^2 < 1$ and denotes the strength of the linear association between E and N. A value of 1 shows that there is a strong positive correlation between the air velocity results of experimental model and the air velocity results of numerical model. A value of zero shows that there is no agreement between the air velocity results of numerical model and the air velocity results of experimental model.

5.2 Nash–Sutcliffe Efficiency (NSE)

Nash–Sutcliffe coefficient (NSE) was first proposed by Nash–Sutcliffe efficiency in 1970 (Nash and Sutcliffe 1970), and since then this method has been frequently used in many studies to evaluate the performance of models. Generally, NSE is used to evaluate the prediction results of models and also used together with MSE to determine accuracy of a model. Small value of MSE tends to follow high NSE and vice versa. NSE should be close to 1 for a good agreement in a model. (For example, NSE values between 0.8 and 1 indicate a perfect matched model.) In this study, Nash–Sutcliffe coefficient is an indicator of numerical model results ability to very closely follow experimental results on the perfect model line in 1:1 line format. It is expressed as follows:

$$\text{NSE} = 1 - \left(\frac{\sum_{i=1}^{n}\left(E_i-N_i\right)^2}{\sum_{i=1}^{n}\left(E_i-\bar{E}\right)^2}\right) \tag{19}$$

where E is the mean air velocity from the results of experimental model, N is the mean air velocity from the results of numerical model, and $\bar{E}$ is the mean of E values.

The range of NSE is between $-\infty$ and 1. When NSE is equal to 1, this corresponds to a perfect match of the numerical model results to experimental model results. The predicted results strongly agree with the observed data if value of NSE is zero, whereas an efficiency which is lower than zero indicated that the observed mean is a better predictor as the model. Our results showed that there exists good agreement with a high NSE in terms of numerical model results and experimental model performance.

6 Results and Discussion

6.1 Comparison of Evaluation Criteria of the Experimental Data and Numerical Models Results

The chamber air velocity of numerical models and experimental models for various water depth and front plate angles is presented in Table 1. The plots of experimental model results versus the numerical model results are shown in Fig. 8 for 64 sets of results.

As can be seen from Fig. 8, model results are found to be scattered around the 45° line (1:1 line). There is good agreement between the mean air velocities and the results of experimental and numerical models based on $R^2 = 0.99$

Table 1 Mean air velocity of experimental and numerical models

Wave series no.	d (cm)	Experimental model results				Numerical model results			
		$\alpha=47°$	$\alpha=40°$	$\alpha=35°$	$\alpha=30°$	$\alpha=47°$	$\alpha=40°$	$\alpha=35°$	30°
1	30	5.99	0.11	0.09	0.08	6.13	0.21	0.13	0.08
1	40	5.87	6.11	0.51	0.35	5.97	6.30	0.61	0.39
1	50	5.50	11.45	9.98	1.20	5.56	12.27	10.04	1.23
1	60	8.50	8.28	11.14	10.33	8.70	8.32	11.07	10.37
2	30	5.03	0.13	0.20	0.04	5.25	0.15	0.26	0.05
2	40	3.95	5.26	0.54	0.22	4.03	5.40	0.64	0.21
2	50	7.09	9.95	9.34	1.78	7.12	10.25	9.40	1.90
2	60	7.29	9.55	10.59	10.42	7.42	9.72	11.02	10.50
3	30	4.96	0.08	0.13	0.01	4.90	0.12	0.23	0.02
3	40	4.16	5.35	0.33	0.10	4.23	5.45	0.35	0.09
3	50	5.21	8.62	6.49	0.86	5.20	8.70	6.50	0.86
3	60	3.31	5.88	8.46	7.56	3.35	5.90	8.52	7.63
4	30	5.15	0.30	0.14	0.13	5.34	0.32	0.12	0.13
4	40	5.18	6.23	0.65	0.44	5.09	6.10	0.68	0.46
4	50	8.19	9.24	8.09	0.95	8.24	9.30	8.01	1.00
4	60	7.31	8.56	11.64	9.96	7.37	9.50	12.29	10.22

and NSE = 0.99, respectively. It is clear that the results of numerical model tend to follow the results of experimental model much closer.

Considering the two evaluation criteria, it can be said that the experimental model results are approximately equal to the numerical model results. As a result, the numerical model results justify the experimental data.

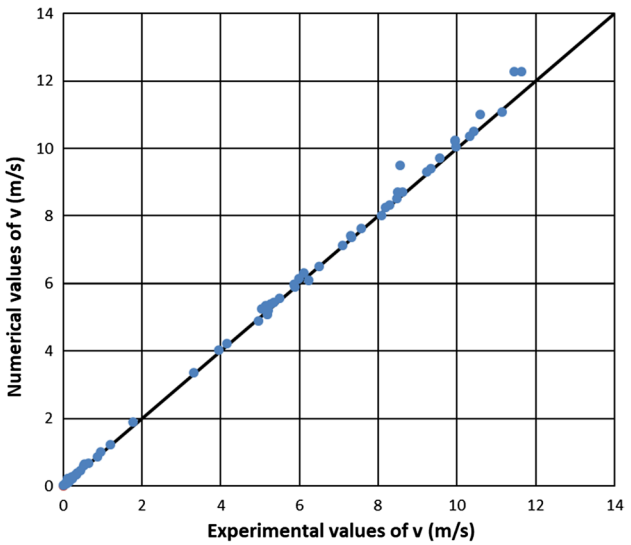

Fig. 8 Verification of experimental and numerical models values for tube air velocity

6.2 Experimental Model Results

In this study, four sets of experiments were performed in order to find an optimum design of OWC structure for chamber geometry by changing the dimensions and front angles. This experiment consisted of four groups where α, e, X variables vary as shown in Fig. 7. As described in Sect. 4, the conclusions are drawn from a combination of four water depths, four regular wave series and four angles. Time series of wave height was measured for each water depth. Also, significant wave height and period were computed from time series of wave height. The wavelength was calculated using Eq. 7. The incident wave heights were recorded without a structure in the channel, hence reducing the influence of wave reflection from the structure. The same test series were repeated with the structure in the channel, and the data of air discharge through the tube at the rear side of the structure were measured.

The procedures and steps described earlier were used to determine wave parameters given in Table 2. This table shows the wave height (H), period (T) and wavelength (L) measured for four different water depths (d).

The experimental study was undertaken under four groups based on chamber geometry and front plate angle as given in Sect. 4, and the details of the results are given as follows for each group.

6.2.1 First Experimental Group

Referring to Fig. 7 for the first experimental group, front plate of the chamber was fixed at an angle of 47° ($\alpha=47°$).

Table 2 Regular wave parameters

No.	H (cm)	T (s)	L (cm)
$d=30$ cm water depth			
1	5.85	1.28	203
2	5.19	1.06	156
3	6.44	0.84	107
4	4.01	2.00	338
$d=40$ cm water depth			
1	6.58	1.28	222
2	6.77	1.07	168
3	6.53	0.84	109
4	4.03	2.01	388
$d=50$ cm water depth			
1	9.89	1.26	229
2	10.64	1.04	165
3	9.92	0.85	112
4	6.01	2.03	433
$d=60$ cm water depth			
1	11.10	1.26	236
2	12.38	1.06	173
3	11.06	0.88	121
4	10.08	1.80	402

The length of the front plate of the chamber (X) and height of opening (e) were 1.02 m and 0.25 m, respectively. The chamber air velocity was measured and also recorded for each water depth with four regular wave sets. The mean and the maximum of air velocity, air outflow, Reynolds number, the mean differential pressure, OWC power and OWC efficiency were calculated. The results of these experiments are shown in Table 3.

As can be seen from Table 3, the Reynolds numbers were calculated for all flow conditions and are found to be greater than 2000. This means that the regime of air flow is fully turbulent. As indicated in Table 3, the calculated η value of 0.0466 was obtained at wave series No. 4 at water depth of 50 cm, which produces the highest value. Additionally, the maximum of mean air outflow rate (Q_{ave}) was found to be 4.30 L/s at the same regular wave condition and water depth. The largest η values were obtained under wave series No. 1 among all water depths, where 50 cm water depth was found to be the best in terms of energy harvesting.

For the first experimental group, differential pressure (ΔP) was calculated from air velocity. ΔP versus t diagram of various water depths and regular wave sets ($4\times4=16$) was then obtained. The ΔP versus t plot for wave series No. 1 is shown in Fig. 9 as an illustrative case. The mean differential pressure of air flow for regular wave series No. 1 is indicated by the red line as depicted in Fig. 9.

6.2.2 Second Experimental Group

In the second experimental group, front plate of the chamber was fixed at an angle of 40° and the water depth was varied to the four levels as explained above. The value of the other parameters of the OWC chamber was taken to be $e=0.41$ m and $x=0.91$ m. The results of the calculated variables using α, e and X are indicated in Table 4. Reynolds

Table 3 Results of calculated values for regular wave series ($\alpha=47°$)

Wave series no.	d (cm)	$V_{ave.}$ (m/s)	$Q_{ave.}$ (L/s)	$Re_{ave.}$	V_{max} (m/s)	Q_{max} (L/s)	Re_{max}	$\Delta P_{ave.}$ (Pa)	P_{owc} (W)	P_w (W)	η
1	30	5.99	3.03	10,032	9.56	4.84	16,002	21.61	0.0656	2.1491	0.0305
1	40	5.87	2.97	9826	10.38	5.26	17,375	20.76	0.0617	2.7189	0.0227
1	50	5.50	2.79	9206	12.10	6.13	20,254	18.22	0.0508	6.0464	0.0084
1	60	8.50	4.30	14,228	13.03	6.60	21,811	43.52	0.1873	7.6164	0.0246
2	30	5.03	2.55	8420	9.24	4.68	15,467	15.24	0.0388	1.4008	0.0277
2	40	3.95	2.00	6612	12.01	6.08	20,103	9.40	0.0188	2.4060	0.0078
2	50	7.09	3.59	11,868	9.82	4.97	16,437	30.28	0.1087	5.7763	0.0188
2	60	7.29	3.69	12,203	10.14	5.14	16,973	32.01	0.1182	7.9704	0.0148
3	30	4.96	2.51	8302	9.47	4.80	15,852	14.82	0.0372	1.7092	0.0218
3	40	4.16	2.11	6963	7.14	3.62	11,951	10.42	0.0220	1.7573	0.0125
3	50	5.21	2.64	8721	8.32	4.21	13,927	16.35	0.0431	4.1037	0.0105
3	60	3.31	1.68	5541	6.47	3.28	10,830	6.60	0.0111	5.2811	0.0021
4	30	5.15	2.61	8620	10.47	5.30	17,525	15.98	0.0417	1.5778	0.0264
4	40	5.18	2.62	8671	11.51	5.83	19,266	16.16	0.0424	1.6015	0.0265
4	50	8.19	4.15	13,709	10.51	5.32	17,592	40.40	0.1676	3.5973	0.0466
4	60	7.31	3.70	12,236	17.93	9.08	30,012	32.19	0.1192	8.9728	0.0133

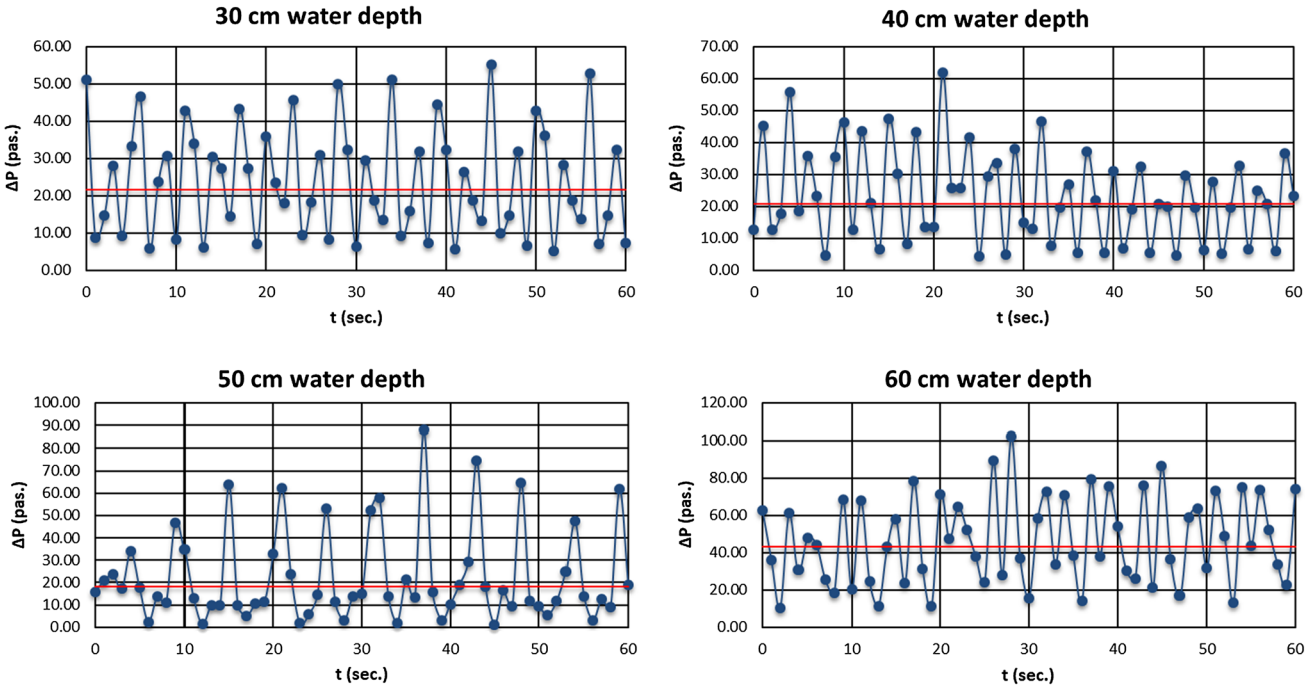

Fig. 9 ΔP versus t diagram for regular wave series No. 1 and $\alpha = 47°$

Table 4 Calculated values for regular wave series ($\alpha = 40°$)

Wave series no.	d (cm)	$V_{ave.}$ (m/s)	$Q_{ave.}$ (L/s)	$Re_{ave.}$	V_{max} (m/s)	Q_{max} (L/s)	Re_{max}	$\Delta P_{ave.}$ (Pa)	P_{owc} (W)	P_w (W)	η
1	30	0.11	0.06	184	0.20	0.10	335	0.01	0.0000	2.1491	0.0000
1	40	6.11	3.09	10,227	14.56	7.37	24,372	22.49	0.0696	2.7189	0.0256
1	50	11.45	5.80	19,166	16.57	8.39	27,736	78.97	0.4579	6.0464	0.0757
1	60	8.28	4.19	13,860	17.80	9.01	29,795	41.30	0.1732	7.6164	0.0227
2	30	0.13	0.07	218	0.22	0.11	368	0.01	0.0000	1.4008	0.0000
2	40	5.26	2.66	8805	10.01	5.07	16,755	16.67	0.0444	2.4060	0.0185
2	50	9.95	5.04	16,655	14.20	7.19	23,769	59.63	0.3005	5.7763	0.0520
2	60	9.55	4.84	15,985	12.47	6.32	20,873	54.94	0.2657	7.9704	0.0333
3	30	0.08	0.04	134	0.17	0.09	285	0.00	0.0000	1.7092	0.0000
3	40	5.35	2.71	8955	14.99	7.59	25,091	17.24	0.0467	1.7573	0.0266
3	50	8.62	4.37	14,429	9.87	5.00	16,521	44.76	0.1954	4.1037	0.0476
3	60	5.88	2.98	9842	8.60	4.36	14,395	20.83	0.0620	5.2811	0.0117
4	30	0.30	0.15	502	0.46	0.23	770	0.05	0.0000	1.5778	0.0000
4	40	6.23	3.16	10,428	14.22	7.20	23,802	23.38	0.0738	1.6015	0.0461
4	50	8.90	4.51	14,897	12.27	6.21	20,538	47.71	0.2151	3.5973	0.0598
4	60	8.56	4.34	14,328	19.07	9.66	31,921	44.14	0.1913	8.9728	0.0213

number was found to be lower than 2000 in the experimental sets with water depth of 30 cm referring to Table 4. Therefore, the regime of the flow is laminar. Since the water depth is less than the height of the opening (i.e., $y = 30$ cm and $e = 41$ cm), the 30 cm water depth has, therefore, the lowest value of the air outflow in this experiment.

The outflow of air is calculated, and the minimum value from calculated mean air outflows was found to be 0.04 L/s as shown in Table 4. This was found at wave series No. 3 and water depth of 30 cm. However, the maximum value of the mean air outflow (5.80 L/s) was found in wave series No. 1 and water depth of 50 cm. Taking Table 4 into consideration,

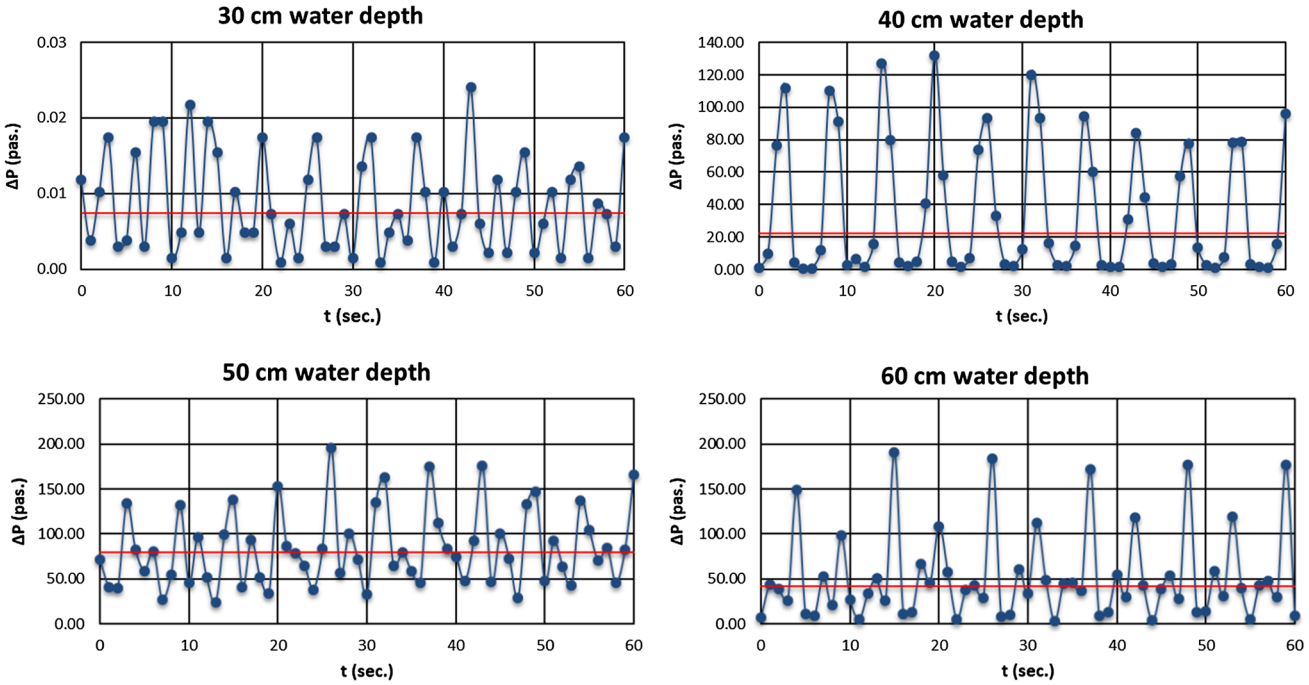

Fig. 10 ΔP versus t diagram for regular wave series No. 1 and $\alpha = 40°$

the maximum efficiency of OWC system was observed at 50 cm water depth and wave series No. 1 with wave characteristics of $H = 9.89$ cm, $T = 1.26$ s and $L = 229$ cm.

In the second experimental group, air velocity for each set of experiments was measured and the value of differential pressure (ΔP) was assessed from air velocity. ΔP versus t diagrams are developed for the various experimental sets of wave series and water depths, and one example is shown in Fig. 10.

Table 5 Calculated values for regular wave series ($\alpha = 35°$)

Wave series no.	d (cm)	$V_{ave.}$ (m/s)	$Q_{ave.}$ (L/s)	$Re_{ave.}$	V_{max} (m/s)	Q_{max} (L/s)	Re_{max}	$\Delta P_{ave.}$ (Pa)	P_{owc} (W)	P_w (W)	η
1	30	0.09	0.05	151	0.30	0.15	502	0.00	0.0000	2.1491	0.0000
1	40	0.51	0.26	854	0.84	0.43	1406	0.16	0.0000	2.7189	0.0000
1	50	9.98	5.05	16,705	20.28	10.27	33,946	59.99	0.3032	6.0464	0.0502
1	60	11.14	5.64	18,647	15.68	7.94	26,246	74.75	0.4217	7.6164	0.0554
2	30	0.20	0.10	335	1.32	0.67	2210	0.02	0.0000	1.4008	0.0000
2	40	0.54	0.27	904	1.54	0.78	2578	0.18	0.0000	2.4060	0.0000
2	50	9.34	4.73	15,634	16.33	8.27	27,334	52.55	0.2486	5.7763	0.0430
2	60	10.59	5.36	17,726	13.86	7.02	23,200	67.55	0.3623	7.9704	0.0455
3	30	0.13	0.07	218	0.49	0.25	820	0.01	0.0000	1.7092	0.0000
3	40	0.33	0.17	552	0.97	0.49	1624	0.07	0.0000	1.7573	0.0000
3	50	6.49	3.29	10,863	14.48	7.33	24,238	25.37	0.0834	4.1037	0.0203
3	60	8.46	4.28	14,161	10.48	5.31	17,542	43.11	0.1847	5.2811	0.0350
4	30	0.14	0.07	234	0.50	0.25	837	0.01	0.0000	1.5778	0.0000
4	40	0.65	0.33	1088	1.15	0.58	1925	0.25	0.0001	1.6015	0.0001
4	50	8.09	4.10	13,542	13.83	7.00	23,150	39.42	0.1615	3.5973	0.0449
4	60	11.64	5.90	19,484	20.75	10.51	34,733	81.61	0.4811	8.9728	0.0536

6.2.3 Third Experimental Group

The mean air velocity, the mean air outflow, Reynolds number and other parameters are shown in Table 5. For this experimental group, the front plate angle of the chamber was fixed at 35°. In addition, the length of the plate and the height of the opening were taken as $X = 0.85$ m and $e = 0.51$ m, respectively, as shown in Fig. 7.

As shown in Table 5, the Reynolds number for the various water depths and wave series for 35° angle indicates that the flow regime is laminar in 30 cm and 40 cm water depths. According to Table 5, a maximum of mean value of the air outflow (Q_{ave}) of 5.90 L/s was found in wave series No. 4 at water depth of 60 cm. However, the minimum Q_{ave} value of 0.05 L/s was observed at wave series No. 1 at 30 cm water depth. Finally, the largest values of OWC efficiency were obtained in wave series No. 1 and at water depth of 60 cm. In other words, the best efficiency is achieved in wave series No. 1 and water depth of $d = 60$ cm.

For this experiment, differential pressure (ΔP) was calculated from air velocity and ΔP versus t diagram was plotted as shown in Fig. 11. From the 16 ΔP versus t diagrams, various sets of wave series and water depths were developed, and an example is shown in Fig. 11.

6.2.4 Fourth Experimental Group

In the final experimental group, front plate of the chamber was fixed at an angle of 30°. The opening height and the front plate length of OWC were taken as 0.60 m and 0.80 m, respectively. The Reynolds number operations that were performed for the third experimental group were repeated for this experimental group. Therefore, Reynolds number was determined for all series in this experiment. Since the water depth (d) is higher than the height of the opening (e), the 60 cm water depth has the highest value of the air outflow in this experiment. In addition, it was also observed from the values of Reynolds number that flow regime was fully turbulent. The lowest value of air outflow was found at the water depth of 30 cm as shown in Table 6.

A minimum mean value of the air outflow (Q_{ave}) of 0.01 L/s was found in wave series No. 3 at water depth of 30 cm, and a maximum value of the mean air outflow (Q_{ave}) of 5.28 L/s was found in wave series No. 2 and at water depth of 60 cm. As can be seen from Table 6, the maximum OWC efficiency was observed at water depth of 60 cm and wave series No. 1 with wave characteristics of $H = 11.10$ cm, $T = 1.26$ s and $L = 236$ cm.

In this final experimental group, differential pressure (ΔP) was calculated from air velocity. From the 16 ΔP versus t diagrams, various sets of wave series and water depths were generated and wave series No. 1 was plotted and is shown in Fig. 12 as an example. The mean differential pressure of air flow for regular wave series No. 1 is indicated by the red line as depicted in Fig. 12.

Among all experimental data, the best results for water depth and wave series with regards to maximum efficiency of OWC system were obtained at 50 cm and wave series

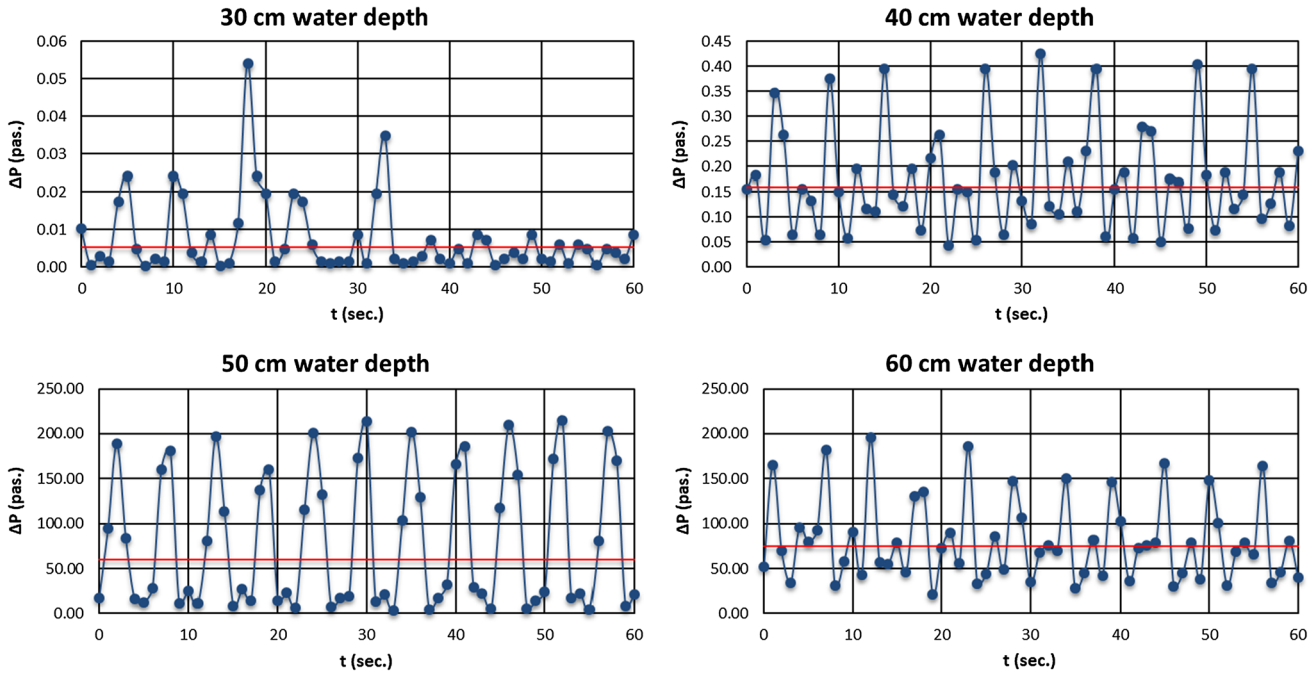

Fig. 11 ΔP versus t diagram for regular wave series No. 1 and $\alpha = 35°$

Table 6 Calculated values for regular wave series (α = 30°)

Wave series no.	d (cm)	$V_{ave.}$ (m/s)	$Q_{ave.}$ (L/s)	$Re_{ave.}$	V_{max} (m/s)	Q_{max} (L/s)	Re_{max}	$\Delta P_{ave.}$ (Pa)	P_{owc} (W)	P_w (W)	η
1	30	0.08	0.04	134	0.22	0.11	368	0.00	0.0000	2.1491	0.0000
1	40	0.35	0.18	586	0.56	0.28	937	0.07	0.0000	2.7189	0.0000
1	50	1.20	0.61	2009	4.16	2.11	6963	0.87	0.0005	6.0464	0.0001
1	60	10.33	5.23	17,291	19.38	9.82	32,440	64.28	0.3363	7.6164	0.0442
2	30	0.04	0.02	67	0.08	0.04	134	0.00	0.0000	1.4008	0.0000
2	40	0.22	0.11	368	0.32	0.16	536	0.03	0.0000	2.4060	0.0000
2	50	1.78	0.90	2979	7.92	4.01	13,257	1.91	0.0017	5.7763	0.0003
2	60	10.42	5.28	17,442	18.14	9.19	30,364	65.40	0.3451	7.9704	0.0433
3	30	0.01	0.01	17	0.04	0.02	67	0.00	0.0000	1.7092	0.0000
3	40	0.10	0.05	167	0.18	0.09	301	0.01	0.0000	1.7573	0.0000
3	50	0.86	0.44	1440	2.03	1.03	3398	0.45	0.0002	4.1037	0.0000
3	60	7.56	3.83	12,654	13.05	6.61	21,844	34.43	0.1318	5.2811	0.0250
4	30	0.13	0.07	218	0.55	0.28	921	0.01	0.0000	1.5778	0.0000
4	40	0.44	0.22	737	0.82	0.42	1373	0.12	0.0000	1.6015	0.0000
4	50	0.95	0.48	1590	2.43	1.23	4068	0.54	0.0003	3.5973	0.0001
4	60	9.96	5.04	16,672	25.52	12.92	42,717	59.75	0.3014	8.9728	0.0336

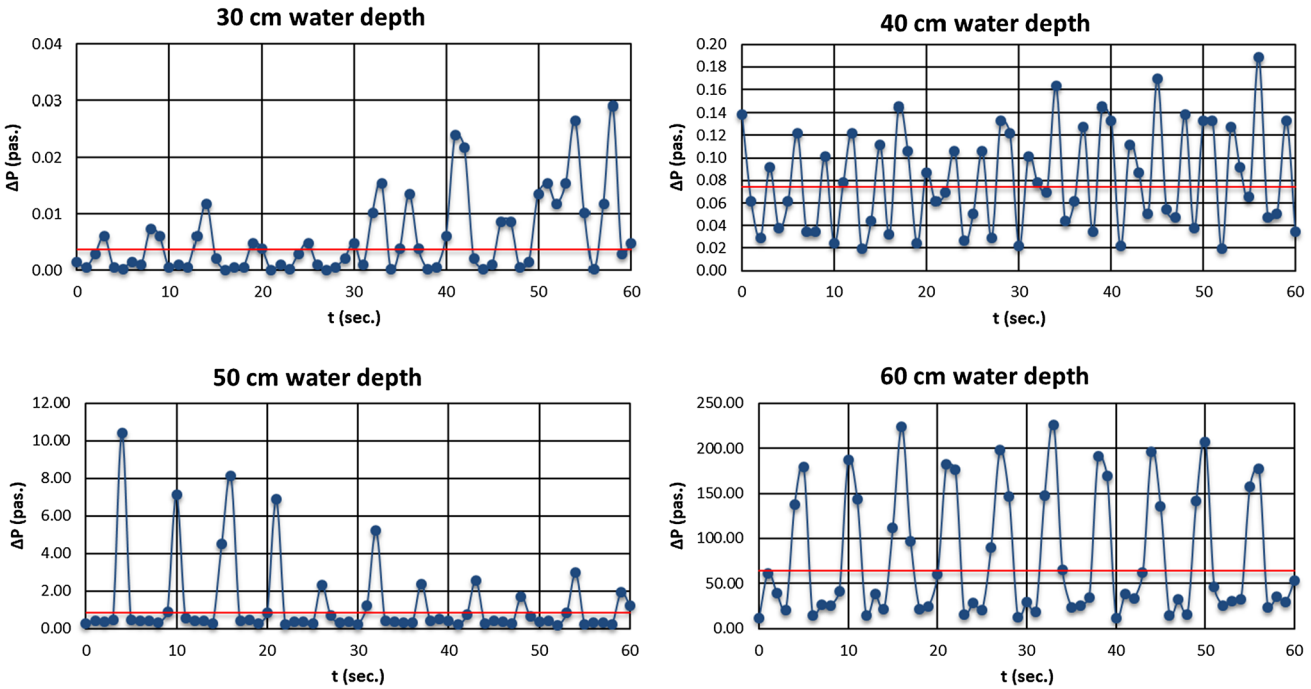

Fig. 12 ΔP versus t diagram for regular wave series No. 1 and $\alpha = 30°$

No. 1, respectively, considering different water depths ($d = 30$, 40, 50 and 60 cm) and the various wave series (No. 1, 2, 3 and 4). Regular wave series and graph of efficiency of OWC system were drawn and are discussed below. According to Fig. 13, the diameter of outflow tube is considered to be constant and for each wave series, maximum efficiency of OWC was seen at 40° angles.

According to the results obtained from Fig. 13, the maximum efficiency of OWC for wave series number 1 and four angles of the front plate of the structure is obtained at an

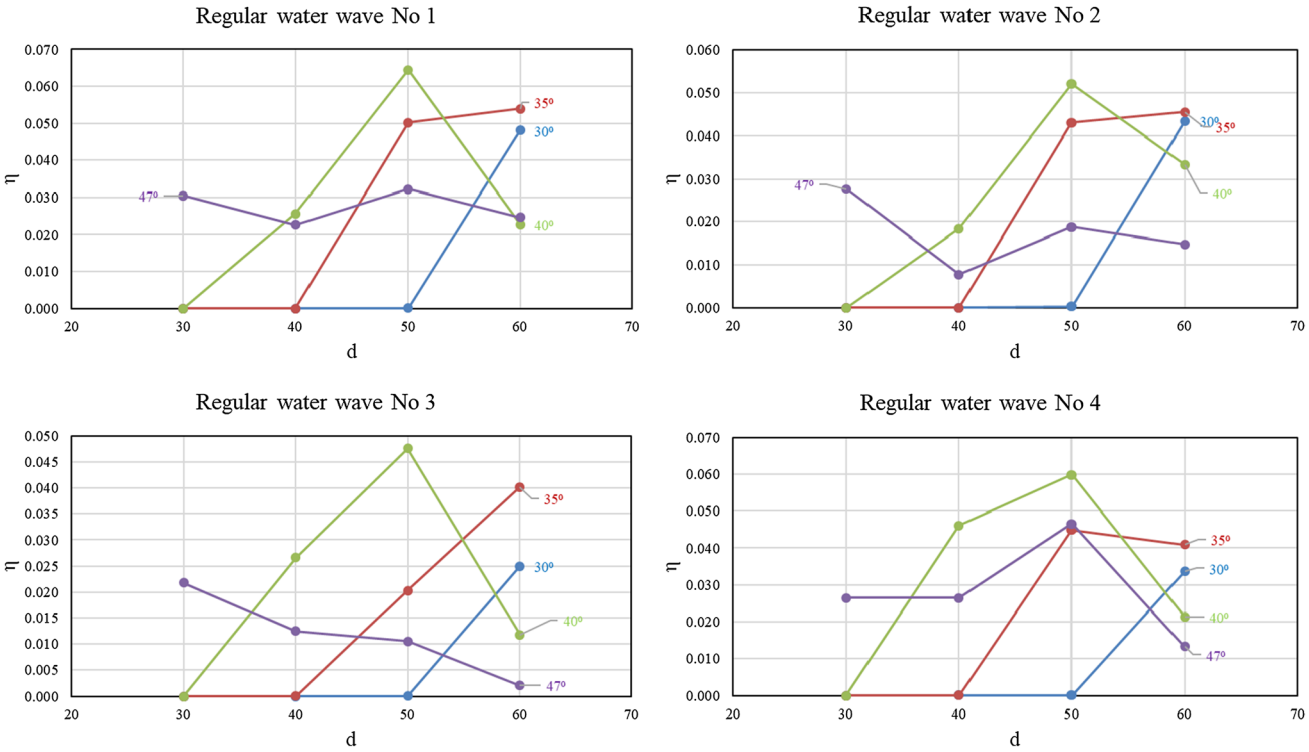

Fig. 13 Average of OWC efficiency (η)—water depth (d) diagram for each wave series

angle of 40° and at a water depth of 50 cm. Also, the maximum OWC efficiency was obtained for wave series number 2, 3 and 4 at 50 cm water depth and 40° angle. By considering these results, the importance of the opening height of the structure is revealed and the structure's maximum efficiency is observed at the opening height of 41 cm. Considering the water depths in Fig. 13, the maximum efficiency in OWC system was observed at 50 cm water depth in wave series No. 1, No. 2, No. 3 and No. 4.

Finally, the experimental results indicate that the chamber geometry and front plate angle of OWC, water depth and wave parameters such as wave height and wave period are important factors for achieving maximum efficiency of OWC system. From the results shown in Tables 3, 4, 5 and 6, the maximum efficiency is observed at regular wave series No. 1, water depth of 50 cm and at an angle of 40°. Considering these results, the characteristics of regular wave series are $H = 9.89$ cm, $T = 1.26$ s and $L = 229$ cm.

7 Conclusions

In this study, the accuracy of the output air velocities measured from the experimental model and obtained from the numerical model were tested by using R^2 and NSA as evaluation criteria. According to the test results, the numerical results and the experimental results match very well ($R^2 = 0.99$ and NSA = 0.99).

A series of experiments were conducted to test the performance of the chamber of OWC system. The influence of water depth and slope of the chamber was also investigated. The importance of the wave series at different depths is shown by analyzing the wave series. The maximum of OWC efficiency in wave series number 1 for all water depths and angles turned out to be 0.0644. The value for wave series number 2 turned out to be 0.0520, with a 19 percent decrease, and the value for wave series number 3 turned out to be 0.0476, with a 26% decrease. In the latest wave series (wave series number 4), the value is 0.0598, with a 7% decrease. Thus, wave series number 1 has a higher efficiency of OWC in comparison with other wave series. According to this result, the importance of the wave characteristics on OWC structure is shown.

The experimental results indicate that the chamber geometry and front plate angle of the OWC system, water depth and wave parameters are important factors to obtain maximum powering in terms of energy harvesting. Not only the positive air (outflow) but also the negative air (inflow) movements through the tube mounted at the rear of the structure were taken into account for different piston types. One of the striking results is that, since the water depth is less than the height of the opening, the observed power value was

minimum in terms of energy harvesting. Therefore, the value of opening height (e) should be at least equal to the water depth. Looking at the results, the maximum of efficiency of OWC is obtained at opening height of 41 cm in the OWC system, because, when height of opening is 41 cm, incident wave affects more on the water level inside the OWC chamber and the oscillation of water is greater. So, air inside the chamber of the OWC system is more compressed and maximum efficiency of the OWC structure is obtained at this height of opening. Considering the results of experimental model, the best results for efficiency of OWC were observed at regular wave series No. 1 for $d = 50$ cm and $\alpha = 40°$.

Acknowledgements This research was funded by TUBITAK (The Turkish National Science and Technology Foundation) under the Grant Number 112M413. The authors are grateful to TUBITAK for supporting our study.

References

Boccotti P (2007) Comparison between a U-OWC and a conventional OWC. Ocean Eng 34:799e805

Bouali B, Larbi S (2013) Contribution to the geometry optimization of an oscillating water column wave energy converter. Energy Procedia 36:565–573

Brito-Melo A, Sarmento AJNA et al. (1999) A 3D boundary element code for the analysis of OWC wave power plants. In: 9th international offshore and polar engineering conference, Brest, France, May 30–June 4, 1999

Clément A (1996) Dynamic non-linear response of OWC wave energy devices. In: Proceedings of the 6th international offshore and polar engineering conference, Los Angeles, California, May 26–31, 1996

Dehdar-Behbahani S, Parsaie A (2016) Numerical modeling of flow pattern in dam spillway's guide wall. Case study: Balaroud dam, Iran. Alex Eng J 55(1):467–473

Dizadji N, Sajadian SE (2011) Modeling and optimization of the chamber of OWC system. Energy 36:2360–2366

El Marjani A, Castro F, Rodriguez MA, Parra MT (2008) Numerical modeling in wave energy conversion systems. Energy 33(8):1246–1253

Evans DV (1982) Wave-power absorption by systems of oscillating surface pressure distributions. J Fluid Mech 114:481–499

Flow Science Inc. (2012) Flow-3D user's manuals. Flow Science Inc., Santa Fe, NM

Folley M, Curran R, Whittaker T (2006) Comparison of LIMPET contra-rotating wells turbine with theoretical and model test predictions. Ocean Eng 33:1056–1069

Hong K, Shin SH, Hong DC, Choi HS, Hong SW (2007) Effects of shape parameters of OWC chamber in wave energy absorption. In: Proceedings of the 17th international offshore and polar engineering conference, Lisbon, Portugal, July 1–6, 2007

International Energy Agency (2005) Energy statistics of non-OECD countries. 2003–2004. IEA, Paris

Josset C, Clément AH (2007) A time-domain numerical simulator for oscillating water column wave power plants. Renew Energy 32(8):1379–1402

Joyce A, Pontes MT, Bettencourt J, Sarmento AJNA, Gato L, Brito-Melo A, Falcão A (1993) Wave tank testing of shoreline OWC power plant. In: Proceedingsof 1st European wave energy symposium, Edinburgh, pp 63–66

Krause P, Boyle DP, Bäse F (2005) Comparison of different efficiency criteria for hydrological model assessment. Adv Geosci 5:89–97

Liu Z, Hyun BS, Hong KY (2008) Application of numerical wave tank to OWC air chamber for wave energy conversion. In: Proceedings of 18th international offshore and polar Engineering conference, Vancouver, Canada, July 6–11, 2008, p 350e6

Luo Y, Nader JR, Cooper P, Zhu SP (2014) Nonlinear 2D analysis of the efficiency of fixed oscillating water column wave energy converters. Renew Energy 64:255–265

Malara G, Arena F (2013) Analytical modelling of an U-oscillating water column and performance in random waves. Renew Energy 60:116–126

Marjani AE, Ruiz FC, Rodriguez MA, Santos MTP (2008) Numerical modelling in wave energy conversion systems. Energy 33:1246e53

Martins E, Silveira Ramos F, Carrilho L, Gato LMC, Justino PAP, Trigo L, Neumann F (2005) CEODOURO project: overall design of a OWC in the new oporto breakwater. In: 6th European wave and tidal energy conference, University of Strathclyde, Glasgow, UK, 2005, pp 273–280

Morris-Thomas MT, Irvin RJ, Thiagarajan KP (2007) An investigation into the hydrodynamic efficiency of an oscillating water column. J Offshore Mech Arct Eng 129:273

Nash JE, Sutcliffe JV (1970) River flow forecasting through conceptual models, part I—a discussion of principles. J Hydrol 10:282–290

Parsaie A, Dehdar-Behbahani S, Haghiabi AH (2016) Numerical modeling of cavitation on spillway's flip bucket. Front Struct Civ Eng 10(4):438–444

Ramandan A, Mohamed MH, Abdien SM, Marzouk SY, El Feky A, El Baz AR (2014) Analytical investigation and experimental validation of an inverted cup float used for wave energy conversion. Energy 70(2014):539–546

Sağlam M, Sulukan E, Uyar TS (2010) Wave energy and technical potential of Turkey. J Naval Sci Eng 6(2):34–50

Sarmento AJNA, Falcao AF (1985) Wave Generation by an oscillating surface pressure and its application in wave-energy extraction. J Fluid Mech 150:467–485

Shore Protection Manual (1984) U.S. Army Coastal Engineering Research Center, Department of the Army, Corps of Engineers, U.S. Govt. Printing Office, Washington, DC, USA, Vol. 1

Texeira P, Davyt DP, Didier E, Ramalhais R (2013) Numerical simulation of an oscillating water column based on Navier–Stokes equations. Energy 61:513–530

Tindall CE, Xu M (1996) Optimizing a wells-turbine-type wave energy system. IEEE Trans Energy Convers 11:631–635

Tseng RS, Wu RH, Huang CC (2000) Model study of a shoreline wave-power system. Ocean Eng 27:801e21

Wang DJ, Katory M, Li YS (2002) Analytical and experimental investigation on the hydrodynamic performance of onshore wave-power devices. Ocean Eng 29(8):871–885

Warner JM (1997) Wave energy conversion in a random sea. Ph.D. thesis, Technical University of Nova Scotia, Halifax, Canada

Zhang Y, Zou Q-P, Greaves D (2012) Air–water two-phase flow modelling of hydrodynamic performance of an oscillating water column device. Renew Energy 41:159–170